CrossMark

ORIGINAL PAPER

# Electrochemical performance of CeO$_2$ nanoparticle-decorated graphene oxide as an electrode material for supercapacitor

Dongyang Deng[1] · Nan Chen[2] · Xuechun Xiao[1] · Shangfeng Du[3] · Yude Wang[2]

**Abstract** Cerium oxide nanoparticles and cerium oxide nanoparticle-decorated graphene oxide (GO) are synthesized via a facile chemical coprecipitation method in the presence of hexadecyltrimethylammonium bromide (CTAB). Nanostructure studies and electrochemical performances of the as-prepared samples were systematically investigated. The crystalline structure and morphology of the nanocomposites were examined by X-ray diffraction (XRD), scanning electron microscopy (SEM), transition electron microscopy (TEM), Raman spectrum, and X-ray photoelectron spectroscopy (XPS). Electrochemical properties of the CeO$_2$ electrode, the GO electrode, and the nanocomposites electrodes were investigated by cyclic voltammetry (CV), galvanostatic charge/discharge (GCD), and electrochemical impedance spectroscopy (EIS) measurements. The CeO$_2$ nanoparticle-decorated GO (at the mole ratio of CeO$_2$/GO = 1:4) electrode exhibited excellent supercapacitive behavior with a high specific capacitance of 382.94 F/g at the current density of 3.0 A/g. These superior electrochemical features demonstrate that the CeO$_2$ nanoparticle-decorated GO is a promising material for next-generation supercapacitor systems.

## Introduction

Environmental concern over the ever-growing energy demands and curtailed fossil fuel resources has provoked the quest for sustainable energy storage devices with enhanced power and energy densities [1, 2]. Supercapacitors, which are one of the most promising candidates for flexible energy storage devices, have attracted considerable attention due to high power density, long cycle life, and excellent charge–discharge rates compared to common batteries [3–5]. The performances of supercapacitors depend mainly on the properties of their active electrode materials, and they can be usually divided into three types including carbon materials, conducting polymers and metal oxides [6]. Among them, nanostructured metal oxides have attracted much attention due to theirs favorable redox potential and conductivity to store electrical charge. Therefore, some typical metal oxides, such as RuO$_2$ [7], MnO$_2$ [8–10], and Co$_3$O$_4$ [11], have been widely investigated as high-capacity electrode materials for supercapacitors. However, several problems such as the high cost, low electrical conductivity, and poor stability limit the practical applications of metal oxides as supercapacitor electrodes. Thus, it is imperative to develop cost-effective, environmentally friendly, and high-performance alternative candidates for supercapacitors.

As one of the most reactive rare earth materials, CeO$_2$ has attracted a great deal of attention due to its extensive applications [12–15]. CeO$_2$ in nanometer size can be considered as one of the promising redox supercapacitor materials since CeO$_2$ is the most abundant, environmental friendly, and least expensive rare earth metal oxide with excellent redox

✉ Shangfeng Du
S.Du@bham.ac.uk

✉ Yude Wang
ydwang@ynu.edu.cn

[1] School of Materials Science and Engineering, Yunnan University, 650091 Kunming, People's Republic of China

[2] Department of Physics, Yunnan University, 650091 Kunming, People's Republic of China

[3] School of Chemical Engineering, University of Birmingham, Edgbaston, Birmingham B15 2TT, UK

characteristics. Furthermore, its nanostructure with superior surface area has prominent effect on pseudocapacitance. Nevertheless, because of the intrinsic poor electrical conductivity of metal oxides, only the surface part of electroactive materials can effectively contribute to the total capacitance and the underneath parts could hardly participate in the electrochemical charge storage process, which severely affects the performance of supercapacitors. One approach in solving this problem is to combine carbon materials with high electrical conductivity and metal oxides as electrodes for supercapacitors. Recently, Dezfuli and coworkers utilized a sonochemical method to synthesize $CeO_2$-reduced graphene oxide (RGO), which showed a specific capacitance of 185 F/g at the current density of 2 A/g [16].

Graphene oxide (GO), which possesses the characteristics of graphene, shows a great promise for the fabrication of nanoscale structures, and more importantly, contains a range of reactive oxygen functional groups (e.g., carboxylic acids, hydroxy, and carbonyl groups). However, the individual GO sheet exhibits a tendency to aggregate and re-stack owing to the interplanar $\pi$–$\pi$ interactions and van der Waals' forces between the graphene layers [3]. This agglomeration reduces the surface area of the GO films and the diffusion of electrolyte ions, which results in a decrease in the electrochemical performance. To avoid the re-stacking, composites made of GO and metal oxides seem to be a good solution. This is beneficial to both materials because of their synergistic effect. Metal oxides prevent GO from agglomeration and re-stacking and also increase the available surface area. Besides, GO helps the formation of metal oxide nanostructures with uniformly dispersed controlled morphologies, suppressing the agglomeration of metal oxides. The oxygen-containing groups within graphene oxide will ensure good electrical contact, interfacial interactions, and bonding between graphene oxide and metal oxide.

In the present work, we use a simple facile chemical coprecipitation method to synthesize $CeO_2$, GO, and $CeO_2$ nanoparticle-decorated GO materials for the application of supercapacitors. The structure, surface morphology, and composition of the as-prepared samples have been fully investigated. The capacitive behaviors of the electrodes were also investigated and compared.

## Experimental

### Materials

The graphene oxide (GO) was prepared according to modified Hummers' method. And the mass concentration of the as-prepared GO is 10 mg/mL. All the other reagents used in the experiments were purchased from commercial sources of analytical grade and used without further purification.

### Preparation of $CeO_2$ nanoparticle-decorated GO

$CeO_2$ nanoparticle-decorated GO at different mole ratio was prepared by a facile chemical coprecipitation method. In brief, 182 mg hexadecyltrimethylammonium bromide (CTAB) was dissolved into 10 mL distilled water with stirring at the temperature of 40 °C until a homogenous solution was obtained. Four hundred thirty-four milligram sample of cerium nitrate hexahydrate was dissolved into 10 mL distilled water with stirring to get transparent solution. Then 10 mL CTAB (0.05 M) was added into the solution dropwise under stirring for 30 min. Next, GO with a certain mole ratio ($n_{CeO_2}/n_{GO}$ =1:1, 1:2, 1:4, 1:5, respectively) was added into the resulting solution with maintaining stirring for 10 min, and the GO was dispersed in the getted solution by ultrasonic vibration for 1 h. An amount of 10 mL of 25 wt% liquor ammonia was added into the resulting suspension dropwise under stirring. After vigorous stirring for 2 h, the suspension was aged for 30 min at room temperature. The resulting products were centrifuged, and the precipitates were thoroughly washed with distilled deionized water and ethanol and dried at 60 °C overnight. For comparison, $CeO_2$ and the GO were also synthesized under the same condition as $CeO_2$ nanoparticle-decorated GO. The resultant products were collected and further characterized.

### Structural and morphology characterization

The crystallographic structures of the materials were determined by Rigaku D/max-3B diffractometer with a copper target and $K_{\alpha 1}$ radiation ($\lambda = 1.54056$ Å) from 10° to 90° in step of 0.01°. Scanning electron microscopy (SEM) images of the morphology of samples were obtained from FEI QUANTA200 with microscope operating at 30 kV. Detailed studies of the microstructure were also carried out by transmission electron microscopy (TEM) (JEOL JEM-2100) at an acceleration voltage of 200 kV. X-ray photoelectron spectroscopy (XPS) was carried out at room temperature in an ESCALAB 250 system.

### Electrochemical measurements

Nickel foam with the size of 1 cm × 2 cm was first pretreated successively with diluted hydrochloric acid and absolute ethanol to ensure a clean surface. The electrodes were fabricated as follows: the as-prepared samples, carbon black, and polyvinylidene fluoride (PVDF) were mixed in a mass ratio of 85:10:5. A small amount of ethanol was added to make a homogeneous mixture. Then the resulting mixture was coated onto the nickel foam substrate, which was followed by drying at 60 °C for 24 h in a vacuum oven. The resulting paste was pressed at 10 MPa. Each electrode contained about 3 mg of

electroactive material and had a geometric surface area of about 1 cm$^2$. A typical three-electrode experimental cell equipped with a working electrode, a platinum foil counter electrode, and a saturated calomel electrode (SCE) was used for measuring the electrochemical properties of the working electrode. All electrochemical measurements were carried out on a CHI 600E electrochemical workstation (ChenHua Instruments, Shanghai) in 6 M KOH aqueous solution as electrolyte at 25 °C. The electrochemical properties of the products were investigated with cyclic voltammetry (CV), galvanostatic charge/discharge (GCD) tests, and electrochemical impedance spectroscopy (EIS) which were obtained using an AC voltage of 5 mV in a frequency range from 0.01 Hz to 100 kHz. The specific capacitances (C, (F/g) ) as shown in Table 1 were calculated according to the following equations:

$$C = \frac{I \times t}{\Delta V \times m} \tag{1}$$

where $I$ (mA) is the constant discharge current, $t$ (s) is the discharging time, $m$ (mg) is the total mass of active materials in both electrodes, and $\Delta V$ (V) is the operating voltage window obtained from the discharge curve excluding the voltage drop.

## Results and discussion

In order to confirm the structure, phase, and purity of the materials, X-ray diffraction patterns (XRD) were recorded for the CeO$_2$ and CeO$_2$ nanoparticle-decorated GO (1:4). As shown in Fig. 1, the curve of CeO$_2$ and CeO$_2$ nanoparticle-decorated GO (1:4) are shown in blue and red, respectively. The short vertical bars in green represent the positions of the Bragg reflections. The diffraction peaks of CeO$_2$ and CeO$_2$ nanoparticle-decorated GO (1:4) coincide well with the standard pattern of CeO$_2$ (JCPDS card no. 81-0792). There is no diffraction peak originating from the GO species in the XRD spectrum of CeO$_2$ nanoparticle-decorated GO (1:4), probably due to the bad crystallinity of GO in the CeO$_2$ nanoparticle-decorated GO (1:4) sample. The characteristics of the XRD pattern demonstrate that GO does not change the crystal structure of CeO$_2$. The width of the diffraction peaks indicates the
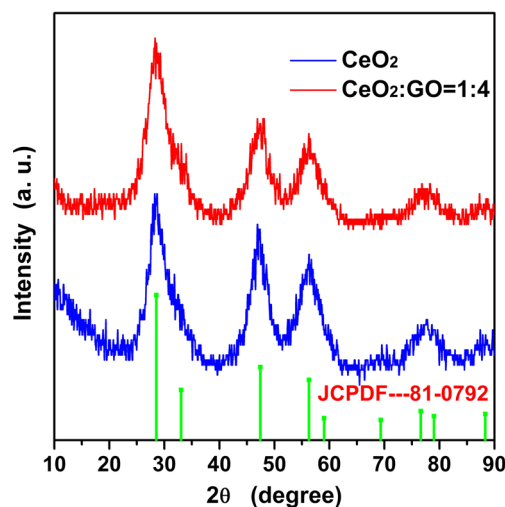


**Fig. 1** XRD pattern of the as-prepared CeO$_2$ and CeO$_2$/GO (1:4)

small average grain size. The average crystal size of CeO$_2$ nanoparticle-decorated GO (1:4) sample is calculated to be 2.31 nm.

Raman spectroscopy is a standard technique for determining the ordered and disordered nature of carbon-based materials. Figure 2 shows the Raman spectra of CeO$_2$ and CeO$_2$ nanoparticle-decorated GO (1:4). One peak at 459.03 cm$^{-1}$ could be seen in the Raman spectra of CeO$_2$ and CeO$_2$ nanoparticle-decorated GO (1:4), which is attributed to the symmetrical stretching mode of the Ce–O$_8$ vibrational unit [16]. Peaks were observed at 1345.85 and 1593.16 cm$^{-1}$ in the CeO$_2$ nanoparticle-decorated GO (1:4) spectrum, which confirmed the D and G bands, respectively. The D band represents sp$^3$ carbon in the graphitic lattice, which is associated with the structural defects such as bond length disorder, bond-angle disorder, and hybridization which can break the symmetry and selection rules, while the G band is related to the in-plane vibration of C sp$^2$ atoms [17–19]. More intensity of the D and G bands can be attributed to the high loading of GO in CeO$_2$ nanoparticle-decorated GO (1:4). Therefore, the result
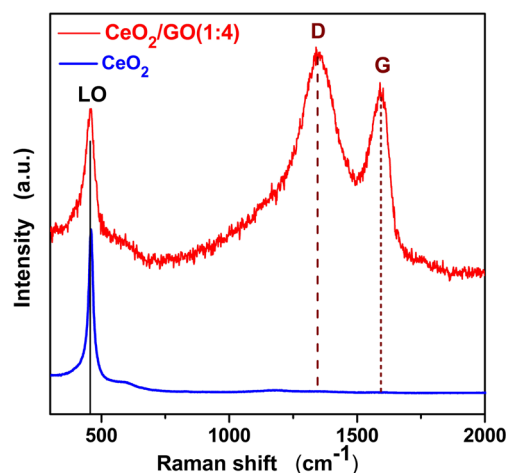
**Table 1** Comparison of capacitance values for CeO$_2$/GO nanocomposites at different molar ratios at 3 A/g

| Materials | Capacitance (F/g) |
|---|---|
| CeO$_2$ | 81.18 |
| GO | 35.12 |
| CeO$_2$/GO (1:1) | 45.29 |
| CeO$_2$/ GO (1:2) | 82.35 |
| CeO$_2$/GO (1:4) | 382.94 |
| CeO$_2$/GO (1:5) | 18.37 |



**Fig. 2** Raman spectra of the as-prepared CeO$_2$/GO (1:4)
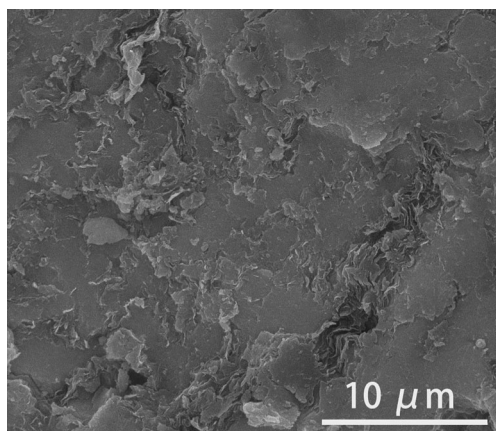
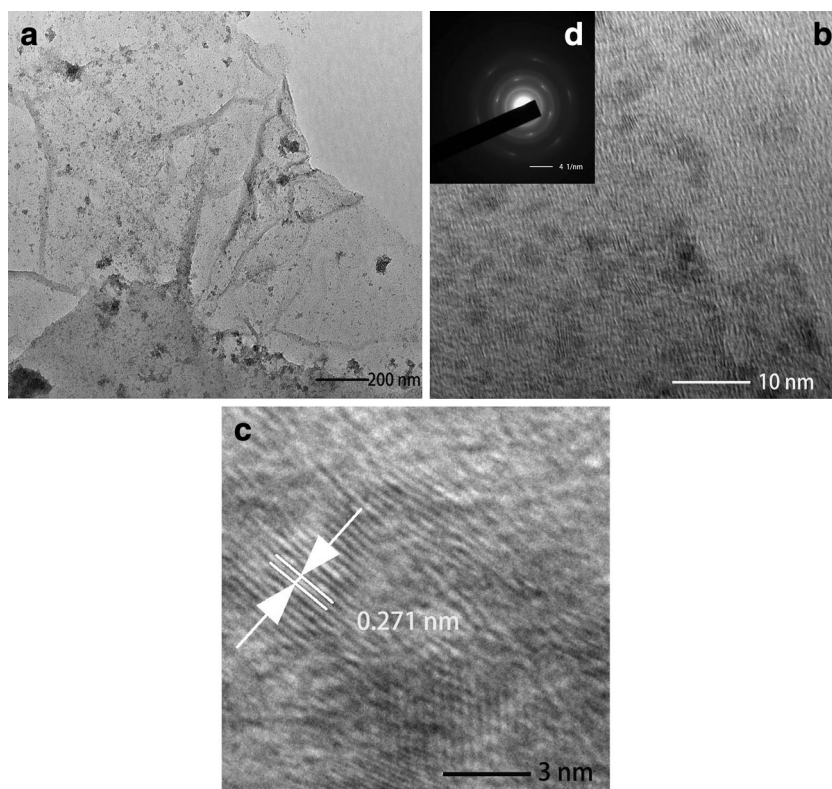**Fig. 3** SEM image of the as-prepared $CeO_2$/GO (1:4)

of the Raman measurement confirms that the $CeO_2$ nanoparticle-decorated GO (1:4) has been formed during the facile chemical coprecipitation treatment.

The morphology of the $CeO_2$ nanoparticle-decorated GO (1:4) sample was characterized using SEM. As shown in Fig. 3, crumpled sheets observed were GO, whereas none $CeO_2$ nanoparticles were observed in $CeO_2$ nanoparticle-decorated GO (1:4) sample. It is probably due to the crystal size of $CeO_2$ that is so small. In order to find $CeO_2$ nanoparticles, the sample was further investigated by TEM and HR-TEM. From Fig. 4a, one can find that the distribution of $CeO_2$ nanoparticles across the surface of the GO sheets is clearly visible, suggesting that the chemical coprecipitation method

is a simple and efficient way of synthesizing $CeO_2$ nanoparticle-decorated GO. In Fig. 4b, $CeO_2$ nanoparticles were uniformly spread throughout the GO sheets. The size of $CeO_2$ is about 2–3 nm, which is in satisfactory agreement with the results from the XRD studies. Furthermore, in Fig. 4d (inset of Fig. 4b), the SAED pattern of the nanocomposite also displayed bright diffraction rings, conforming the growth of polycrystalline $CeO_2$ on the graphene sheets [19]. As shown in Fig. 4c, the HR-TEM image of the $CeO_2$ nanoparticle-decorated GO (1:4) sample shows the orientation of grains in different directions, and the lattice fringes are clearly visible with space of 0.271 nm corresponding to the (200) planes of $CeO_2$.

XPS was employed to characterize the surface chemical compositions and the valence states of the as-synthesized $CeO_2$ nanoparticle-decorated GO (1:4), as shown in Fig. 5. As is shown in Fig. 5a, one finds that the C1s consists of three components: C–C (284.67 eV), C–O (286.25 eV), and C=O (287.98 eV). This spectrum was fully consistent with those reported previously [20]. The high-resolution XPS spectrum of O1s is shown in Fig. 5b. Especially, the state of O1s indicates that there are two sorts of oxygen on the surface. One is the lattice oxygen ($O_{lattice}$) and the other is adsorbed oxygen ($O_x^-$). The peaks of adsorbed oxygen and lattice oxygen are shown at binding energies of 531.24 and 529.08 eV, respectively [21]. $O_{lattice}$ is attributed to the oxygen ions in the crystal lattice which are thought to be pretty stable and have no contribution to the reactions on the electrode. Meanwhile, $O_x^-$ is
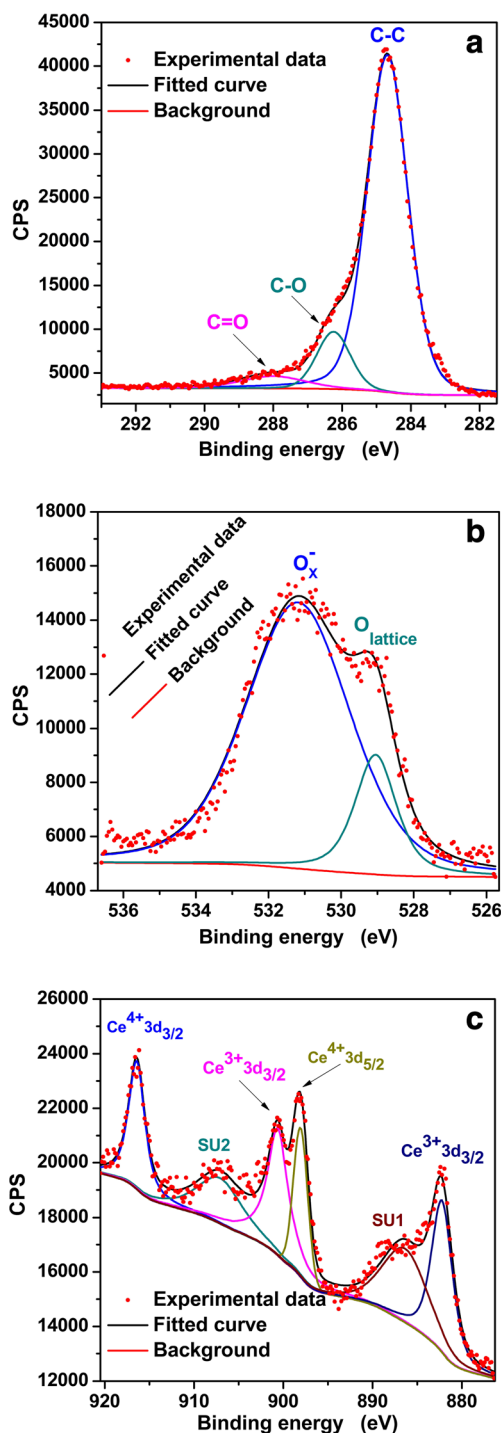
**Fig. 4** TEM images of the as-prepared $CeO_2$/GO (1:4)

**Fig. 5** The high-resolution XPS survey spectra of C 1s (**a**), O 1s (**b**), and Ce (**c**) of the as-prepared CeO$_2$/GO (1:4)

as-prepared CeO$_2$ nanoparticle-decorated GO (1:4) exhibited amazing electrochemical properties. The Ce3d core level peak can be confirmed by XPS analysis, as shown in Fig.5c. Due to its highly non-stoichiometric nature, Ce atoms with both 3+ and 4+ valences are presented in CeO$_2$ nanoparticle-decorated GO (1:4). The main peaks of Ce$^{4+}$ 3d$_{3/2}$ and Ce$^{4+}$ 3d$_{5/2}$ are shown at binding energies of 917.49 and 898.18 eV, respectively. Those of Ce$^{3+}$ 3d$_{3/2}$ and Ce$^{3+}$ 3d$_{3/2}$ are located at 900.62 and 882.40 eV, respectively. Two additional satellite lines SU1 and SU2, which means "shake-up," are shown at 886.63 and 916.49 eV, respectively. To rationalize XPS findings, one can state that the presence of Ce$^{3+}$ is a result of oxygen vacancies and this effect is enhanced in nanoparticles because a larger fraction of the atoms is on the surface as the particle size is reduced and the surface atoms have reduced coordination [22]. The oxygen vacancies that lead to the transformation between Ce$^{4+}$ and Ce$^{3+}$ may be a key issue in reactions on the electrode. Through calculating the ratio of peak areas, one can find that the mole ratio of Ce$^{3+}$/Ce$^{4+}$ is 1.59 for CeO$_2$ nanoparticle-decorated GO (1:4). It is obvious that CeO$_2$ nanoparticle-decorated GO (1:4) sample has a strong oxygen storage and release capacity via the redox shift between Ce$^{4+}$ and Ce$^{3+}$ under oxidizing and reducing conditions, respectively.

To test the supercapacitive performance of pure CeO$_2$, GO, and CeO$_2$ nanoparticle-decorated GO (1:4) electrodes, CV was firstly recorded in a three-electrode system using saturated calomel electrode (SCE) as the reference and platinum foil as the counter electrode. The capacitive behavior of pure CeO$_2$, GO, and CeO$_2$ nanoparticle-decorated GO (1:4) electrodes was systematically examined in this work and typical CV curves of pure CeO$_2$, GO, and CeO$_2$ nanoparticle-decorated GO (1:4) measured at 10 mV/s in 6 M KOH which are shown in Fig. 6a. The CV curves show that CeO$_2$ nanoparticle-decorated GO (1:4) nanocomposite electrode has the largest enclosed area, compared with CeO$_2$ and GO electrodes, exhibiting the highest specific capacitance. We just qualitatively describe the electrochemical performance of the CeO$_2$ nanoparticle-decorated GO (1:4) electrode, CeO$_2$ nanoparticle electrode, and GO electrode by the CV curve. And then we use GCD tests to quantificationally describe the specific capacitance of electrodes. In the CeO$_2$ nanoparticle-decorated GO (1:4) sample, the synergistic effect is found by combining CeO$_2$ and GO, which reasonably resulted from the uniform dispersion of CeO$_2$ nanocrystals onto the surface of GO sheets and better electronic conductivity of the GO. Hence, a high electrochemical performance can be achieved. Figure 6b shows the CV curves of CeO$_2$ nanoparticle-decorated GO (1:4) electrode at different scan rates of 5, 10, 20, 50, and 100 mV/s in a potential range of 0 to 0.51 V. One pair of redox peaks is observed in every CV curve, which reveals that the capacitance characteristic of CeO$_2$ nanoparticle-decorated GO (1:4) sample is typical
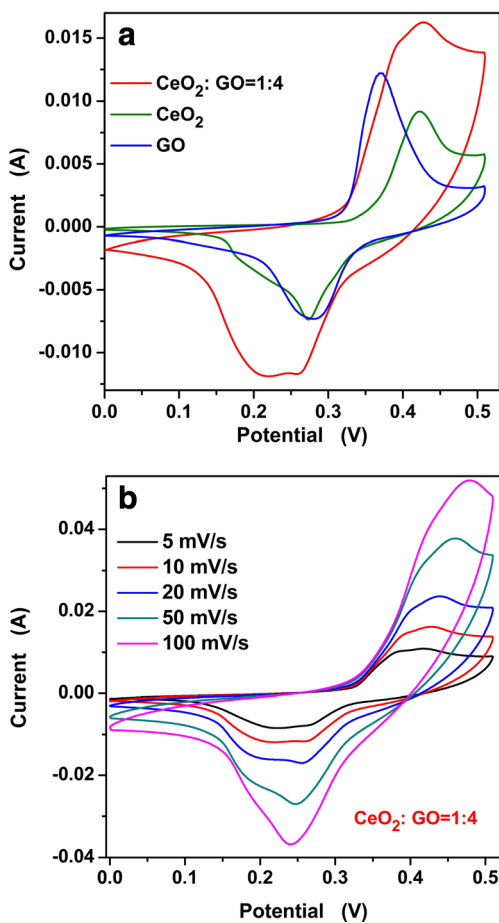
attributed to the absorbed oxygen ions, which is active in reactions on the electrode. Through calculating the areas of $O_x^-$ and O$_{lattice}$ emission lines, the concentrations of $O_x^-$ and O$_{lattice}$ to O1s are estimated to be 83.44 and 16.56 %, respectively. As one can see, the percentage of $O_x^-$ is so large, which may be a key issue in reactions on the electrode. Therefore, the

**Fig. 6 a** CV curves of pure CeO₂, GO, and CeO₂/GO (1:4) nanoparticle electrodes at 10 mV/s; **b** CV curves of CeO₂/GO (1:4) nanoparticle electrode at different scan rates

**Fig. 7 a** Charge-discharge curves of pure CeO₂, GO, and CeO₂/GO nanoparticle electrodes at 3 A/g; **b** charge-discharge curves of CeO₂/GO (1:4) nanoparticle electrode at 3~15 A/g

pseudocapacitance. At low scan rates (5–20 mV/s), no curve shows significant changes in the shape with increasing scan rate, indicating highly reversible redox reactions. This shows stability of electrolytes in the supercapacitor. However, the shape of the CV curves is slightly distorted as the scan rate increase, especially at a high scan rate of 100 mV/s.

The charge–discharge curves of the as-synthesized materials are shown in Fig. 7. Charge–discharge curves of CeO₂, GO, and CeO₂ nanoparticle-decorated GO at 3.0 A/g are shown in Fig. 7a. The discharge-specific capacitance values of CeO₂, GO, and CeO₂ nanoparticle-decorated GO (1:4) calculated from the discharge curves are 81.18, 35.12, and 382.94 F/g at the current density of 3.0 A/g, respectively. One can see that the specific capacitance of the as-prepared CeO₂ nanoparticle-decorated GO (1:4) nanocomposite sample was 990.37 % higher than that of GO electrode and 371.72 % higher than that of CeO₂ electrode, respectively. The result quantificationally expresses the meaning of compositing CeO₂ and GO. The specific capacitance values of CeO₂ nanoparticle-decorated GO nanocomposites at different mole ratio at the current density of 3.0 A/g are shown in Table 1. Among the obtained samples, the CeO₂ nanoparticle-
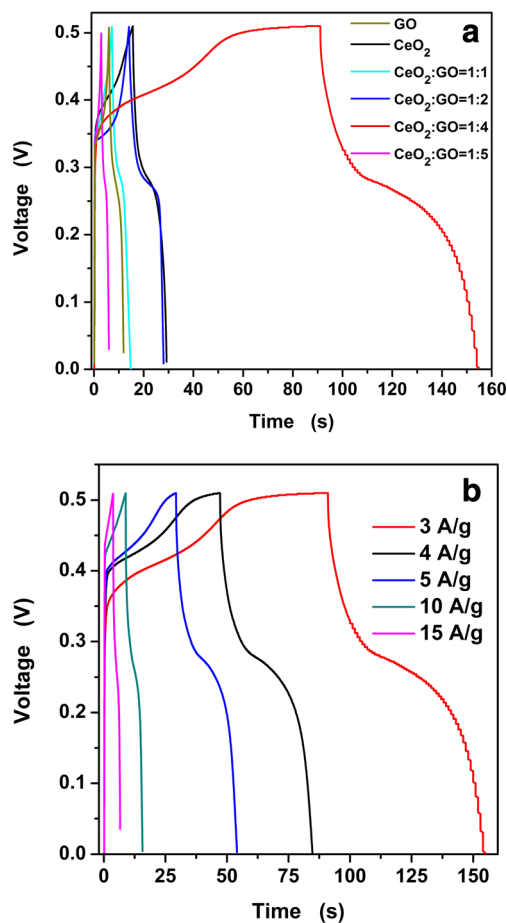
decorated GO (1:4) exhibits the best electrochemical performance and the specific capacitance value can be reached to 382.94 F/g at the current density of 3.0 A/g. According to the results in Table 1, the composition of CeO₂/GO composites plays a significant role in specific capacitance. In Fig. 4, one can see that the size of CeO₂ is about 2–3 nm, so the number of the particles is large. When the content of GO is less, there is not enough GO to provide support for CeO₂; small CeO₂ particles cannot be evenly dispersed on the GO. So the specific capacitance is lower. When the molar ratios of CeO₂/GO reaches 1:4, there is enough GO to provide support for CeO₂. The synergistic effect is found by combining CeO₂ and GO, which reasonably resulted from the uniform dispersion of CeO₂ nanocrystals onto the surface of GO sheets and better electronic conductivity of the GO. Hence, a high electrochemical performance can be achieved. Continuing increasing the amount of the GO, the individual GO sheet exhibits a tendency to aggregate and re-stack owing to the interplanar π–π interactions and van der Waals forces between the GO layers. The agglomeration reduces the surface area of the GO films and the diffusion of electrolyte ions, which results in a decrease in the electrochemical performance. Moreover, the

agglomeration of GO sheets cut off the contact between electrolyte and cerium oxide on the surface of the folding covers, resulting in a loss of the specific capacitance. Figure 7b shows the galvanostatic charge/discharge (GCD) curves of the $CeO_2$ nanoparticle-decorated GO (1:4) electrode in the 0–0.51 V potential window. The value of specific capacitance calculated by the GCD method for $CeO_2$ nanoparticle-decorated GO (1:4), at current densities of 3.0, 4.0, 5.0, 10.0, and 15.0 A/g, was found to be 382.94, 295.69, 244.12, 137.06, and 85.68 F/g, respectively. Besides, the specific capacitance values of $CeO_2$ nanoparticle-decorated GO (1:4) are much higher than the other $CeO_2$-based electrode materials, as shown in Table 2 [16, 23–34].

The calculated specific capacitance values as a function of current density for $CeO_2$, GO, and $CeO_2$ nanoparticle-decorated GO (1:4) sample are shown in Fig. 8. For the red curve, it can be observed that the specific capacitance decreases with the increasing current density from 3.0 to 15.0 A/g. Generally, the rate capability is heavily dependent
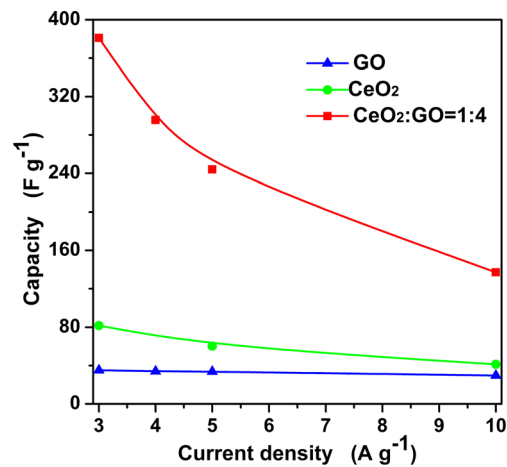


**Fig. 8** Specific capacitance of $CeO_2$, GO, and $CeO_2$/GO (1:4) nanoparticle electrodes as a function of current density

on three processes: the ion diffusion in the electrolyte, the surface adsorption of ions on the electrode materials, and the charge transfer in the electrode. The specific capacitance

**Table 2** Comparison of capacitance values for various structural morphologies of $CeO_2$-based electrodes

| Materials | Capacitance (F/g) | Current density (A/g) or scan rates (mV/s) | electrolyte | References |
|---|---|---|---|---|
| Graphene-ceria | 110 | 10 mV/s | 1 M $H_2SO_4$ | [23] |
| Pure $CeO_2$ | 75 | | | |
| $CeO_2$ | 57 | 5 mV/s | 3 M KOH | [24] |
| $CeO_2$-deposited 3D graphene | 208 | 1 A/g | | |
| Graphene/$CeO_2$ | 89.0 | 1 A/g | 2 M KOH | [25] |
| $CeO_2$–RGO | 185 | 2 A/g | 0.5 M $Na_2SO_4$ | [16] |
| Fe/$CeO_2$-decorated carbon nanofibers | 56 | Not given | 1 M KOH | [26] |
| $CeO_2$/activated carbon | 243 | 1 A/g | 1 M $H_2SO_4$ | [27] |
| Ag/$CeO_2$/rGO | 432.82 | 1 A/g | 3 M KOH | [28] |
| $CeO_2$ octahedron @$MnO_2$ | 178.5 | 0.25 A/g | 1 M $Na_2SO_4$ | [29] |
| $CeO_2$ nanowire @$MnO_2$ | 255.2 | | | |
| $CeO_2$/$Fe_2O_3$ composite nanospindles | 142.6 | 5 mV/s | 6 M KOH | [30] |
| Carbon-coated $CeO_2$ nanorods | 644 | 0.5 A/g | 3 M KOH | [31] |
| Porous carbon/cerium oxide nanoparticle | 150 | 0.25 A/g | 1 M $TEABF_4$ in acetonitrile | [32] |
| Hexagonal $CeO_2$ nanoparticles (CTAB) | 320 ± 3 | 2 A/g | $K_2SO_4$ | [33] |
| NiO–$CeO_2$ | 314 | 1 A/g | 3 M KOH | [34] |
| $CeO_2$ | *81.18* | *3 A/g* | 6 M KOH | *This work* |
| | 60.37 | 5 A/g | | |
| | 41.39 | 10 A/g | | |
| GO | 35.12 | 3 A/g | | |
| | 33.73 | 5 A/g | | |
| | 29.63 | 10 A/g | | |
| $CeO_2$/GO (1:4) | *382.94* | *3 A/g* | | |
| | 295.69 | 4 A/g | | |
| | 244.12 | 5 A/g | | |

decreases with increasing current density owing to reduced penetration of electrolyte into the pores of electrode materials [35].

The EIS analysis is an important technique for investigation of the supercapacitive performance and typical resistance of electrode materials for supercapacitors. The Nyquist impedance plots for $CeO_2$, GO, and $CeO_2$ nanoparticle-decorated GO (1:4) electrodes in 6 M KOH solutions over the frequency range from 0.01 to 100 kHz are shown in Fig. 9. The plots are composed of a line in the lower frequency region. However, there is no small semicircle at high frequency region. The straight line of the Nyquist plot at high frequency is related to the Warburg resistance resulting from the frequency dependence of ion diffusion/transport in the electrolyte [20, 36]. The large Warburg region of these electrodes shows the greater variations in ion diffusion path lengths and increased obstruction of ion movement. The more vertical shape, indicating fast diffusion of ions in electrolyte during charge/discharge process, is an ideally capacitive behavior [37]. The presence of GO with high electrical conductivity resulted in a lower resistance of charge transfer. The EIS result is in good agreement with the CV and GCD results.

The advantages of composite electrode $CeO_2$ nanoparticle-decorated GO (1:4) over the pure $CeO_2$ and GO were clearly demonstrated. Additionally, the cycling stability of the $CeO_2$ nanoparticle-decorated GO (1:4) electrode in 6 M KOH solution between 0 to 0.51 V was investigated at a current density of 5.0 A/g. As shown in Fig. 10, the capacitive retention was about 86.05 % after 500 cycles, indicating a good cycling ability of the composite materials. Before 100 cycles, the support GO allowed the deposition of the $CeO_2$ nanoparticle on the surfaces of GO sheets, which would enhance the mechanical strength of composite materials, resulting in the long charge/discharge cycling ability. After 250 cycles, the specific capacitance suffers a decline. The electrode materials were synthesized by a simple facile chemical coprecipitation
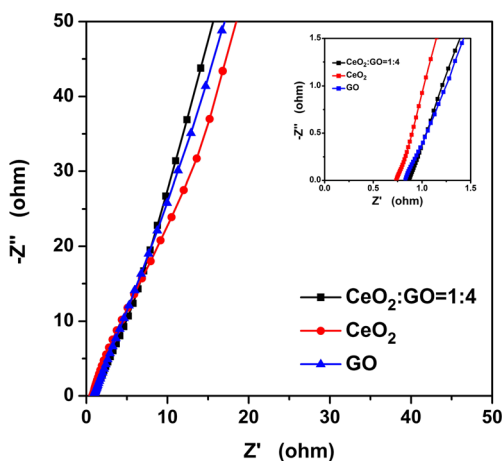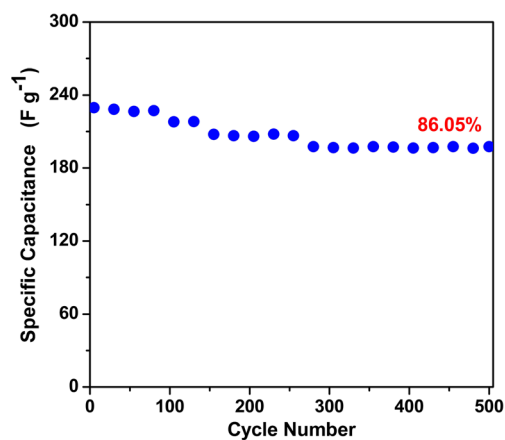


**Fig. 10** Cycling performance of $CeO_2$/GO (1:4) nanocomposite electrode at the current density of 5 A/g

method at room temperature. Due to the relatively low reaction temperature and the short aging time (just 30 min), the size of $CeO_2$ particles is very small that helps to get a higher specific capacitance compared with other methods in the literature as shown in Table 2. At the same time, the small size of $CeO_2$ particles could not guarantee long-term stability and superior cycling performance. The goodish cyclic stability exhibited by the $CeO_2$ nanoparticle-decorated GO (1:4) sample reveals that it is possible to use the nanocomposite in practical energy storage systems.

## Conclusions

The nanostructured $CeO_2$ nanoparticle-decorated GO (at different molar ratio) materials have been synthesized by a simple and inexpensive chemical coprecipitation method. The samples were systematically characterized by XRD, SEM, TEM, XPS, and Raman spectrum. The size of $CeO_2$ nanoparticle in $CeO_2$ nanoparticle-decorated GO (1:4) sample was about 2–3 nm. Electrochemical investigations reveal that $CeO_2$ nanoparticle-decorated GO (1:4) electrode can offer high specific capacitance (382.94 F/g at the current density of 3.0 A/g), attributing to the contributions of the good electrical conductivity of GO and the pseudocapacitance of the $CeO_2$ nanoparticles. Additionally, over 86 % of the original capacitance was retained after 500 cycles, indicating a good cycle stability of composite materials. These results show that a new class of material with high electrochemical performance has been identified.



**Fig. 9** Nyquist plots of $CeO_2$, GO, and $CeO_2$/ GO (1:4) nanocomposite electrodes

# References

1. Hadjipaschalis I, Poullikkas A, Efthimiou V (2009) Renew Sust Energ Rev 13:1513–1522
2. ZN Y, Tetard L, Zhai L, Thomas J (2015) Energ Environ Sci 8:702–730
3. Shao YL, El-Kady MF, Wang LJ, Zhang QH, Li YG, Wang HZ, Mousaviae MF, Kaner RB (2015) Chem Soc Rev 44:3639–3665
4. Ji ZY, Shen XP, Zhou H, Chen KM (2015) Ceram Int 41:8710–8716
5. Khan M, Tahir MN, Adil SF, Khan HU, Siddiqui MRH, Al-warthan AA, Tremel W (2015) J Mater Chem A 3:18753–18808
6. González A, Goikole E, Barrena JA, Mysk R (2016) Renew Sust Energ Rev 58:1189–1206
7. Devadas A, Baranton S, Napporn TW, Coutanceau C (2011) J Power Sources 196:4044–4053
8. Lu Q, Zhou YK (2011) J Power Sources 196:4088–4094
9. Cheng Q, Tang J, Ma J, Zhang H, Shinya N, Qin LC (2011) Carbon 49:2917–2925
10. Xia H, Wang Y, Lin JY, Lu L (2012) Nanoscale Res Lett 7:1–10
11. Kumar M, Subramania A, Balakrishnan K (2014) Electrochim Acta 149:152–158
12. Xiao GL, Li S, Li H, Chen LQ (2009) Micropor Mesopor Mat 120:426–431
13. Tang LG, Yamaguchi D, Burke N, Trimm D, Chiang K (2010) Catal Commun 11:1215–1219
14. XH L, Huang X, Xie XL, Zheng DZ, Liu ZQ, Liang CL, Tong YX (2010) Langmuir 26:7569–7573
15. Meng FM, Zhang C, Fan ZH, Gong JF, Li AX, Ding ZL, Tang HB, Zhang M, Wu GF (2015) J Alloy Compd 647:1013–1021
16. Dezfuli AS, Ganjali MR, Naderi HR, Norouzi P (2015) RSC Adv 5:46050–46058
17. Joung D, Singh V, Park S, Schulte A, Seal S, Khondaker SI (2011) J Phys Chem C 115:24494–24500
18. Srivastava M, Das AK, Khanra P, Uddin ME, Kima NH, Lee JH (2013) J Mater Chem A 1:9792–9801
19. Jiang LH, Yao MG, Liu B, Li QJ, Liu R, Yao Z, SC L, Cui W, Hua X, Zou B, Cui T, Liu BB (2013) CrystEngComm 15:3739–3743
20. Zhang JT, Jiang JW, Zhao XS (2011) J Phys Chem C 115:6448–6454
21. Machocki A, Ioannides T, Stasinska B, Gac W, Avgouropoulos G, Delimaris D, Grzegorczyk W, Pasieczna S (2004) J Catal 227:282–296
22. Li H, Wang GF, Zhang F, Cai Y, Wang YD, Djerdj I (2012) RSC Adv 12:12413–12423
23. Saravanan T, Shanmugam M, Anandan P, Azhagurajan M, Pazhanivel K, Arivanandhan M, Hayakawad Y, Jayavel R (2015) Dalton Trans 44:9901–9908
24. Wang Y, Guo CX, Liu JH, Chen T, Yang HB, Li CM (2011) Dalton Trans 40:6388–6391
25. Chen KF, Xue DF (2015) J Colloid Interf Sci 446:77–83
26. Ghouri ZK, Barakat NAM, Alam AM, Park M, Han TH, Kim HY (2015) Int J Electrochem Sci 10:2064–2071
27. Aravinda LS, UdayaBhat K, Bhat BR (2013) Mat Lett 112:158–161
28. Zheng L, Zhang GN, Zhang M, Guo SH, Liu ZH (2013) J Power Sources 201:376–381
29. Vanitha M, Keerthi, Cao P, Balasubramanian N (2015) J Alloy Compd 644:534–544
30. Zhu SJ, Jia JQ, Wang T, Zhao D, Yang J, Dong F, Shang ZG, Zhang YX (2015) Chem Commun 51:14840–14843
31. Arul NS, Mangalaraj D, Ramachandran R, Grace AN, Han JI (2015) J Mat Chem A 3:15248–15258
32. Padmanathan N, Selladurai S (2014) RSC Adv 4:6527–6534
33. Shuvo MAI, Karim H, Islam MT, Rodriguez G, Nandasiri MI, Schwarz AM, Devaraj A, Noveron JC, Vijayakumar M, Lin YR (2015) Evaluat Energ System 9439:94390H-1-8
34. Maheswari N, Muralidharan G (2015) Energ Fuel 29:8246–8253
35. Kumar R, Agrawal A, Nagarale RK, Sharma A (2016) J Phys Chem C 120:3107–3116
36. Pasta M, Mantia FL, LB H, Deshazer HD, Cui Y (2010) Nano Res 3:352–458
37. Wang XW, Liu SQ, Wang HY, Tu FY, Fang D, Li YH (2012) J Solid State Electrochem 16:3593–3602